Near-Field Ground Motions from the July 2019 Ridgecrest, California, Earthquake Sequence

Susan E. Hough*[1], Eric Thompson[2], Grace A. Parker[3], Robert W. Graves[1], Kenneth W. Hudnut[1], Jason Patton[4], Timothy Dawson[4], Tyler Ladinsky[4], Michael Oskin[5], Krittanon Sirorattanakul[6], Kelly Blake[7], Annemarie Baltay[3], and Elizabeth Cochran[1]

Abstract

The 2019 Ridgecrest, California, earthquake sequence, including an M_w 6.4 event on 4 July and an M_w 7.1 approximately 34 hr later, was recorded by 15 instruments within 55 km nearest-fault distance. To characterize and explore near-field ground motions from the M_w 6.4 foreshock and M_w 7.1 mainshock, we augment these records with available macroseismic information, including conventional intensities and displaced rocks. We conclude that near-field shaking intensities were generally below modified Mercalli intensity 9, with concentrations of locally high values toward the northern and southern termini of the mainshock rupture. We further show that, relative to near-field ground motions at hard-rock sites, instrumental ground motions at alluvial near-field sites for both the M_w 6.4 foreshock and M_w 7.1 mainshock were depleted in energy at frequencies higher than 2–3 Hz, as expected from ground-motion models. Both the macroseismic and instrumental observations suggest that sediments in the Indian Wells Valley experienced a pervasively nonlinear response, which helps explain why shaking intensities and damage in the closest population center, Ridgecrest, were relatively modest given its proximity to the earthquakes.

Cite this article as Hough, S. E., E. Thompson, G. A. Parker, R. W. Graves, K. W. Hudnut, J. Patton, T. Dawson, T. Ladinsky, M. Oskin, K. Sirorattanakul, *et al.* (2020). Near-Field Ground Motions from the July 2019 Ridgecrest, California, Earthquake Sequence, *Seismol. Res. Lett.* **91**, 1542–1555, doi: 10.1785/0220190279.

Introduction

An M_w 6.4 earthquake occurred at 17:33:49 (UTC; 10:33:49 local time) on 4 July 2019, the largest earthquake in southern California in almost 20 yr (Fig. 1). At 03:19:53 (UTC) on 6 July (20:19:53 local time on 5 July), an M_w 7.1 earthquake occurred in proximity to the initial event (Fig. 1). The earthquakes ruptured a complex network of orthogonal faults with predominantly strike-slip mechanisms (see Ross *et al.*, 2019 for an overview).

Following convention, we refer to the M_w 6.4 as a foreshock to the M_w 7.1 mainshock. The foreshock generated surface rupture on a southwest–northeast-trending cross fault (Fig. 2a); the mainshock generated surface rupture on a southeast–northwest-trending fault (Fig. 2a) (Brandenberg *et al.*, 2019). Both the foreshock and the mainshock were very widely felt across the region, with felt shaking from the mainshock extending into Arizona, Nevada, and Utah (Fig. 1). Both earthquakes were recorded by over 500 strong-motion instruments within 300 km, but only by 12 instruments within 55 km near-fault distance (Table 1; see also Data and Resources), and 30 stations within 100 km. The sparsity at close distances reflects the history of the naval base at China Lake, which was established in the 1940s in a remote location to serve as a weapons development and testing facility. The data are, therefore, too sparse to address one of the key questions raised by the sequence: was the observed damage in the town of Ridgecrest (population 28,000; nearest-fault distance ~15 km) consistent with expectations given the magnitudes and distances of the events? Although single-family wood-framed houses are known to generally perform well in earthquakes (Brandenberg *et al.*, 2019), in the popular press, the limited extent of damage in Ridgecrest was portrayed as a surprise (e.g., Lin, 2019). Indeed, there was little if any damage to masonry chimneys around the town or to evaporative coolers installed on many roofs. Even at modified Mercalli intensity (MMI) 7, some chimneys are expected to break; intensity prediction equation (IPE) of Atkinson and Wald (2007) predicts average mainshock

1. U.S. Geological Survey, Pasadena, California, U.S.A.; 2. U.S. Geological Survey, National Earthquake Information Center, Golden, Colorado, U.S.A.; 3. U.S. Geological Survey, Menlo Park, California, U.S.A.; 4. California Geological Survey, Sacramento, California, U.S.A.; 5. Earth and Planetary Sciences Department, Earth and Physical Sciences, University of California, Davis, Davis, California, U.S.A.; 6. Division of Geological and Planetary Sciences, California Institute of Technology, Pasadena, California, U.S.A.; 7. Geothermal Program, Naval Air Weapons Station, China Lake, California, U.S.A.

*Corresponding author: hough@usgs.gov

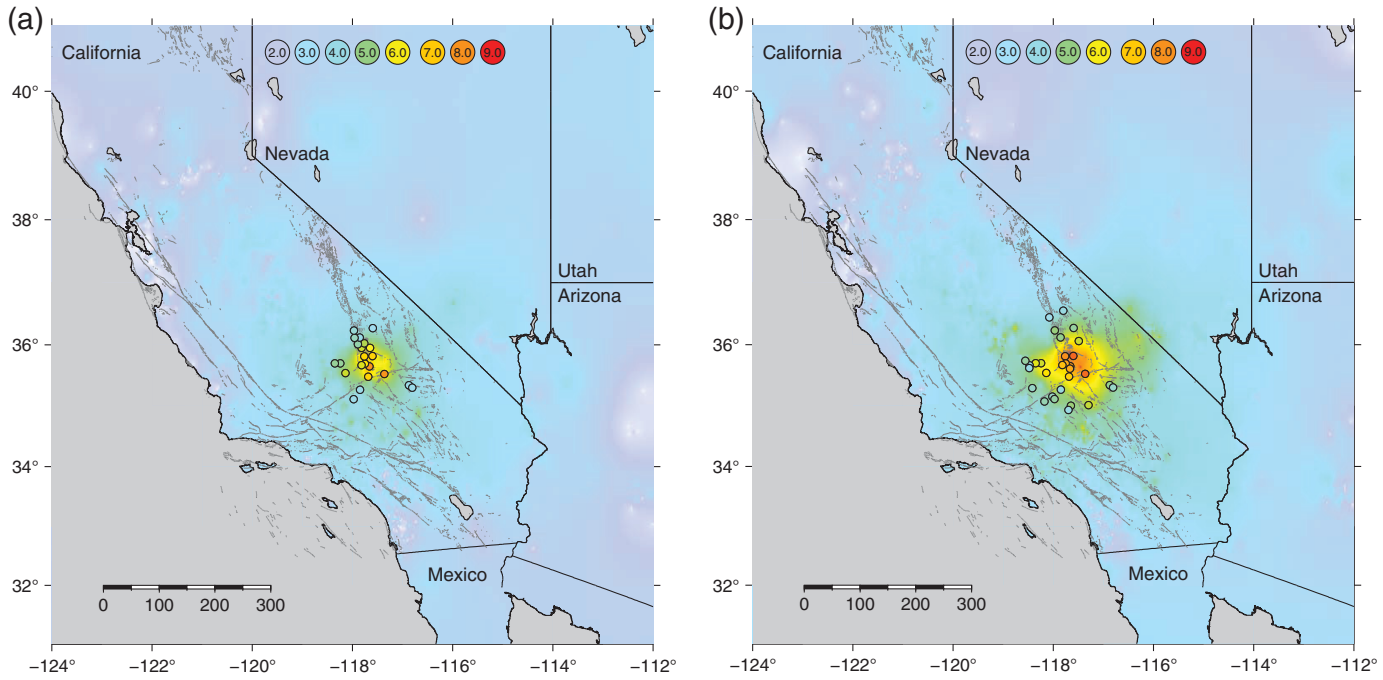

Figure 1. (a) Shaking intensity (modified Mercalli intensity [MMI]) map for the 4 July 2019, M_w 6.4 foreshock, constrained primarily from "Did You Feel It?" (DYFI) intensity data, augmented by near-field intensities assigned via direct survey (this study), with mathematical interpolation between control points. Instrumental intensities for stations within 100 km, estimated from recorded peak ground acceleration (PGA) using the Worden *et al.* (2012) intensity prediction equation, are also shown (filled circles). (b) Similar plot for the 6 July 2019 M_w 7.1 mainshock.

shaking intensities of 7–8 in parts of Ridgecrest. The lack of damage to chimneys and other vulnerable structures suggests that shaking intensities did not reach such levels in either the foreshock or the mainshock. To explore the near-source ground motions, and to better understand the complex source processes of the earthquake, we augment the instrumental data with other data that can constrain ground motions. Other data types include macroseismic intensities estimated from responses to the U.S. Geological Survey (USGS) "Did You Feel It?" (DYFI) system (Wald *et al.*, 1999), intensities estimated from direct ground surveys, and documented environmental effects that can provide a quantitative estimate of peak ground acceleration (PGA). We summarize these observations in this report, including overviews of intensity data, instrumental data, and relevant geological observations.

Intensity Data

Over 54,000 and 44,000 DYFI responses were received, respectively, for the M_w 6.4 foreshock and M_w 7.1 mainshock. From user-supplied questionnaires, the system calculates a community internet intensity (CII) using an algorithm that was designed to be consistent with conventional MMI values, drawing on the community decimal intensity scale introduced by Dengler and Dewey (1998). Apart from values at large distances, which can be elevated by reporting biases (Boatwright and Phillips, 2017), CII values have been shown to provide a surprisingly good indication of PGA (Atkinson and Wald, 2007; Worden *et al.*, 2012) and are used to help constrain USGS ShakeMaps in regions with sparse instrumental coverage (Worden and Wald, 2016). Even in populated places where instrumental coverage is relatively dense, DYFI data provide far better spatial coverage (e.g., Hauksson *et al.*, 2008). The lower total number of responses for the larger mainshock was due to an overload of demand that caused the USGS website to go down in the immediate aftermath of the mainshock. It is impossible to know how many responses were lost, or how responses for the mainshock might have been affected by the occurrence of the widely felt foreshock. Previous studies (e.g., Atkinson and Wald, 2007; Worden *et al.*, 2012) suggest that, potentially complicating issues notwithstanding, spatially rich DYFI data do provide a robust indication of instrumental shaking intensity measures. The DYFI system calculates CII values within postal ZIP codes as well as within geocoded cells, parameterized using hypocentral distance. To explore the near-field distribution of intensities, we focus on CIIs estimated in 1 km geocoded cells. Two DYFI reports yielded near-field mainshock CII values near five from the algorithm but are discounted here because the reports described only environmental effects—rock falls and "fissures"—that past studies have shown are not necessarily reliable indicators of overall shaking intensity (e.g., Brazlee, 1979; Fig. 2a). For simplicity, we refer to all intensity values determined in this study as MMI.

We also consider the difference in near-field CII values from the mainshock and foreshock, calculated using equation (1) for

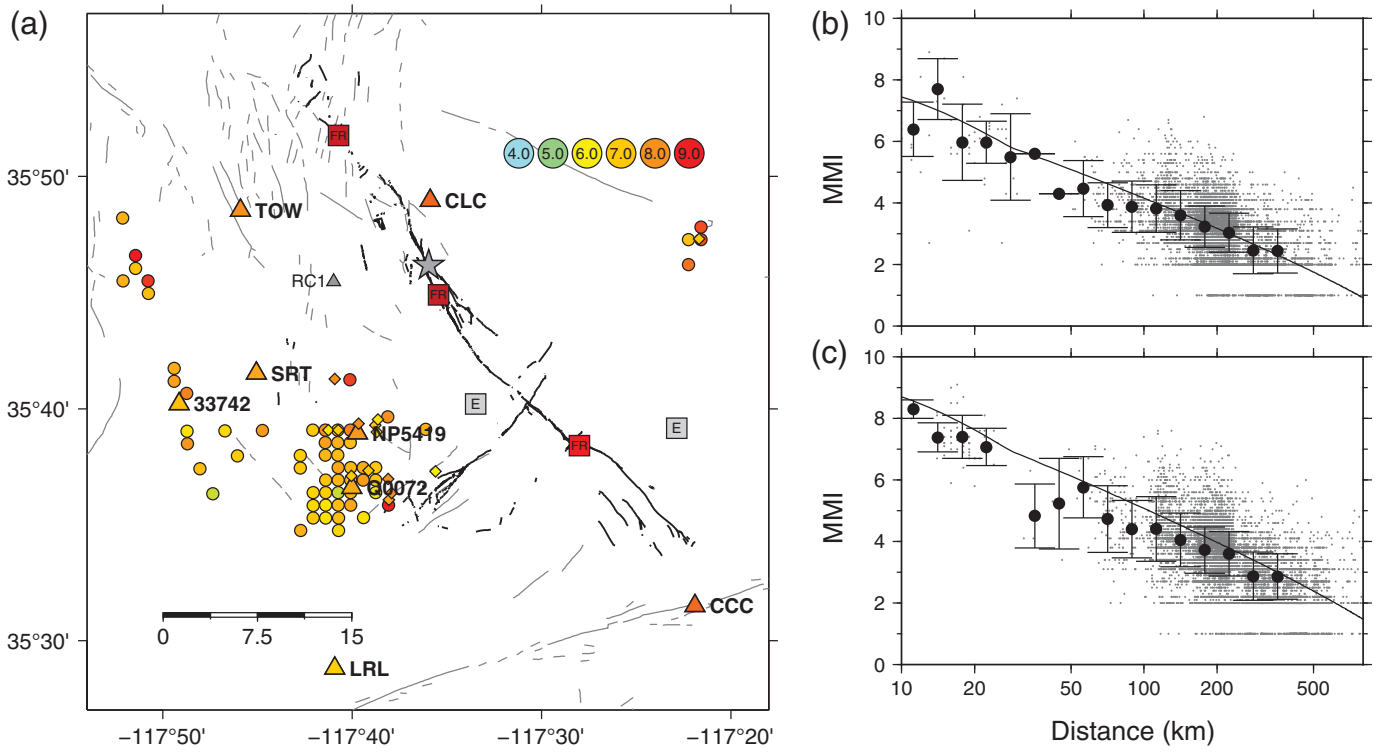

all 1 km geocoded cells for which intensities are available for both events.

$$\delta\mathrm{CII} = \mathrm{CII}_{\mathrm{M}\,7.1} - \mathrm{CII}_{\mathrm{M}\,6.4}. \quad (1)$$

The predicted difference can be calculated using the IPE of Atkinson and Wald (2007). At distances of ~20 km, δCII is predicted to be approximately 1.3 units. This corresponds to a factor of ~2 differences in PGA (Hough, 2000; Worden *et al.*, 2012). For the overall 1 km geocoded data set, observed δCII values are consistent on average, with a high degree of scatter, with predictions. Within 20 km, however, observed δCII values, constrained by over 250 responses in the town of Ridgecrest, are lower than predictions, averaging ~0.5 units rather than 1.3 units. Considering the DYFI reports for both the foreshock and the mainshock separately (Fig. 2b,c), the values for the foreshock are consistent on average with predictions for M_w 6.4, whereas the values for the mainshock tend to follow below predictions for M_w 7.1 at near field (distances). The average intensity for Ridgecrest, constrained by over 250 reports, was 7.1 for the mainshock; the predicted value is closer to 8. Two first-order effects may account in part for the low observed intensities: source-controlled directivity and distance. The M_w 6.4 foreshock ruptured toward the southern edge of Ridgecrest, and central Ridgecrest is closer to the extended rupture of the M_w 6.4 foreshock than to the mainshock rupture, although the northern part of town is roughly equidistant from the nearest approach of both ruptures.

Figure 2. (a). Near-field shaking intensities (color scale indicated) for M_w 7.1 mainshock (epicenter indicated by gray star) determined using DYFI data (small circles), instrumental PGA values (triangles), displaced rock observations (red squares marked FR), and locations where DYFI reports indicated environmental effects that do not reliably constrain intensity (gray squares marked E). Small gray triangle indicates portable station RC1, deployed during the 1995 Ridgecrest sequence (Hough, 1997). (b) 1 km geocoded DYFI intensities for the M_w 6.4 foreshock (small gray dots) and bin-averaged values ± one standard deviation (large black dots). Solid line shows predicted intensities for M 6.4 using intensity prediction equation of Atkinson and Wald (2007). (c) Same plot as (b), for M_w 7.1 mainshock, with predicted intensities for M_w 7.1.

We also conducted a ground survey of local effects to augment DYFI data in parts of Ridgecrest where no, or limited, DYFI data were available (Table 2) and estimated MMI values to the nearest 0.5 unit (Table 2). All values are likely uncertain to ±0.5 units, as is typical for intensities (e.g., Hough and Page, 2011). The goals of the study were to spot-check DYFI results and fill in gaps in spatial coverage. We use the detailed guidelines developed for the European Macroseismic Scale (EMS-98; Grünthal, 1998) to inform these assignments; EMS-98 intensities are expected to be consistent with MMI assignments (Musson *et al.*, 2010). Our intensity values assigned from ground surveys are also generally consistent with DYFI values. At one site—the local animal shelter—the MMI estimate is lower (8.0) than a nearby DYFI value (9.0). The higher DYFI

TABLE 1
Instrumental Data (M_w 7.1)

Station	Latitude (°N)	Longitude (°W)	R_{JB} (km)	PGA_1 (m/s^2)	PGA_2 (m/s^2)	PGA_v (m/s^2)	R_{PGA}	I_{PGA}	PGV (cm/s)	I_{PGV}	Site Geology	V_{S30} (m/s)
CCC	35.525	117.365	2	5.56	4.66	3.39	1.51	8.6	77.67	8.9	Soft rock	432
CLC	35.816	117.598	3	5.01	4.74	3.53	1.38	8.4	42.35	8.0	Hard rock	1464
TOW2	35.809	117.765	9	4.28	3.94	3.52	1.17	8.1	51.98	8.3	Thin all	
NP5419	35.649	117.662	11	3.56	3.58	4.36	0.82	7.9	44.45	8.1	Alluvium	D
WMF	36.118	117.855	16	0.59	0.58	0.58	1.01	5.0	7.61	5.7	Rock	
SRT	35.692	117.751	16	2.37	3.07	2.16	1.26	7.6	42.13	8.0	Alluvium	D
Q0072	35.610	117.667	16	2.98	2.98	3.78	0.79	7.6	29.29	7.5	Alluvium	D
33742	35.670	117.819	22	2.28	2.35	1.48	1.56	7.2	24.45	7.3	Thin all	D
LRL	35.480	117.682	27	1.91	1.97	1.18	1.64	6.9	12.11	6.3	Hard rock	511
MPM	36.058	117.489	28	0.88	0.87	0.88	0.99	5.6	11.95	6.3	Thin all	D
43148	36.228	117.970	31	0.63	0.63	0.55	1.15	5.1	11.51	6.2	Alluvium	D
DAW	36.271	117.592	38	0.57	0.51	0.57	0.95	4.9	3.02	4.4	Soft rock	
WBS	35.537	118.140	54	1.62	1.58	1.62	0.99	6.6	9.53	6.0	Hard rock	402
WOR	35.696	118.242	49	0.90	0.90	0.69	1.30	5.6	4.35	4.9	Hard rock	
DTP	35.267	117.846	53	0.33	0.30	0.30	1.05	4.1	5.79	5.3	Hard rock	

V_{S30} indicates time-averaged shear-wave velocity in the upper 30 m, or estimated National Earthquake Hazards Reduction Program site class, if either estimate is available. These estimates are provided by the strong-motion data center (see Data and Resources); they have not yet been investigated systematically. PGA_1, PGA_2, and PGA_v are recorded peak accelerations on two horizontal components and the vertical component, respectively. R_{PGA} is the ratio between the peak recorded horizontal PGA and PGA_v. R_{JB} indicates estimated nearest-fault distance from each station to the M_w 7.1 mainshock (see Data and Resources). PGA, peak ground acceleration; PGV, peak ground velocity.

estimate may reflect severe damage sustained by several mobile homes in the vicinity, including one that was thrown off of its supports entirely; nearby conventional single-family homes did not reveal damage commensurate with MMI 9. We note that the DYFI questionnaire does not include questions that would differentiate between house types, so intensities can tend to be inflated by reports of damage to mobile homes.

The closest structures to the southwest terminus of the M_w 6.4 rupture are several adjacent properties owned by the Bureau of Land Management (BLM), including several small buildings at the Salt Wells Fire Station, and a nearby structure at the BLM Wild Horse and Burro Corral. The local BLM facilities manager reported that one manufactured building on jacks rocked and may have shifted very slightly, but otherwise effects from both earthquakes were limited to a few broken glasses, with no motion or damage to furniture, appliances, etc. We estimate MMI 6.0 at the cluster of BLM structures.

Overwhelmingly, intensities estimated from direct surveys overlap with and are consistent with DYFI intensities within 1 km; in these cases, the ground-based surveys provide no additional useful information. In Table 2, we include brief summaries of effects at locations where the ground survey did provide useful additional information. We also include summaries of effects on the Navy Base that were described in publicly available news articles with sufficient detail to allow an intensity to be estimated. Because full damage reports have not been made available for base structures, these estimates are considered preliminary and could be revised if more detailed information is released. We note, however, that estimated intensities on the base are consistent with a handful of DYFI responses that were received from nearby locations.

Instrumental Data

Although the focus of this report is understanding near-field ground motions and damage, it is illuminating to consider instrumental parametric data at near and regional distances to explore how the ground motions compare to established ground-motion prediction equations (GMPEs). For these comparisons, we focus on comparisons with the Boore *et al.* (2014) GMPE (hereinafter BSSA14), which we take as a representative model from the suite available for southern California. We do not expect model sensitivity because the differences between existing models are relatively small given the observed aleatory variability of ground motions. For example, the Next Generation Attenuation-West2 Project (NGA-West2) models are within a factor of 2 for PGA at short distances (Gregor *et al.*,

TABLE 2
Damage Observations

Location	Latitude (°)	Longitude (°)	MMI	Summary
Base chapel	33.6549	117.6463	7.0	Reported in news: structural damage (crack in one wall), significant damage to altar
Dolphin and San Bernardino Boulevard	35.6011	117.6344	7.5	Mobile home thrown off supports (red tagged); chimneys not damaged on nearby conventional single-family houses
900 Block of Lamb Road, Ridgecrest	35.606	117.632	8.0	Mobile home thrown off supports; supports showed signs of pounding
Ridgecrest independent	35.6183	117.6672	7.0	Ceiling tiles fell, some computer monitors fell, one plate glass window broken, many things fell
BLM facilities (fire station and horse corral)	35.6217	117.5933	6.0	Few small objects fell, one trailer on jacks apparently shifted slightly, no appliances or furniture displaced; no cracks to interior walls or stucco
Lucky lLiquor	35.6514	117.6878	6.5	Many bottles thrown off shelves and broken
Napa Auto	35.6514	117.6790	7.0	Many items thrown from shelves; shelves (not on wheels) moved sideways ~0.6 m
Animal shelter	35.6163	117.6349	8.0	Some cracks in some cinder-block walls, animal cages moved into room, many objects fell
Mint shop	35.6222	117.6525	7.0	"Everything fell" (bottles, merchandise on shelves), no structural damage, no cracks observed inside or outside
Coso Geothermal Plant	36.014	117.800	6.0	No structural damage, computer monitors knocked over, some small objects fell
Pioneer Plant Market, Trona	35.7886	117.3613	7.0	Merchandise knocked off shelves, no damage to small concrete-block structure
China Lake Hangar 3, Armitage Field, NAWS	35.688	117.682	8.0	Structural cracking throughout hangar and software activity spaces, bolts sheared off support beams, stairwells damaged, seismic joint failure, fixtures on bracing snapped
Michelson Lab, China Lake NAWS	35.656	117.661	8.0	Major cracks in foundation, signs of stress to columns and beams, extensive damage to equipment and offices. Worst damage to Wing 8, three-story building housing machine shop
NAWS Commissary	35.650	117.645	6.5	Ceiling tiles fell, merchandise fell from shelves
Richmond School, China Lake NAWS	35.659	117.644	6.5	Some ceiling tiles fell, some small objects fell

BLM, Bureau of Land Management; MMI, modified Mercalli intensity; NAWS, Naval Air Weapons Station.

2014). BSSA14 is parameterized using the distance from each site to the surface projection of the finite-fault rupture (the Joyner–Boore distance; Joyner and Boore, 1981). In Figure 3, we compare the observed data to BSSA14 predictions for three values of V_{S30}, the time-averaged shear-wave velocity in the upper 30 m: 760 m/s (soft rock), 420 m/s (the estimated average value for all stations), and 275 m/s sediments. We note here that V_{S30} is recognized to be an imperfect proxy for geotechnical properties that will control ground motions. We further note that some of the V_{S30} values have been estimated from a general geological assessment, which do not always compare well with measured values.

Figure 3 confirms that average PGA and peak ground velocity (PGV) values for both earthquakes are generally consistent with BSSA14 GMPE predictions. To consider near-field ground motions, we first estimate instrumental intensities, MMI_i, using the PGA–MMI relation determined by Worden *et al.* (2012). Using this relation, recorded PGA values imply the near-field intensity values given in Table 1 and shown in Figure 2a. The highest recorded PGA, at station CCC, corresponds to MMI_i 8.6. (The PGV–MMI relation from Worden *et al.* (2012) yields consistent instrumental intensities, generally within 0.5 intensity units [Table 1]. In this case, the highest MMI_i value is 8.9). Although sparse, these values are consistent with directly estimated DYFI intensities (Fig. 2a). Considering mainshock PGA values (Table 1), on soft- and hard-rock sites, PGA is generally higher on the horizontal components than the vertical component, whereas on alluvial sites, PGA on the horizontal component is generally closer to or even lower than on the vertical component.

To explore the frequency content of mainshock ground motions, we further consider single-station horizontal-to-vertical

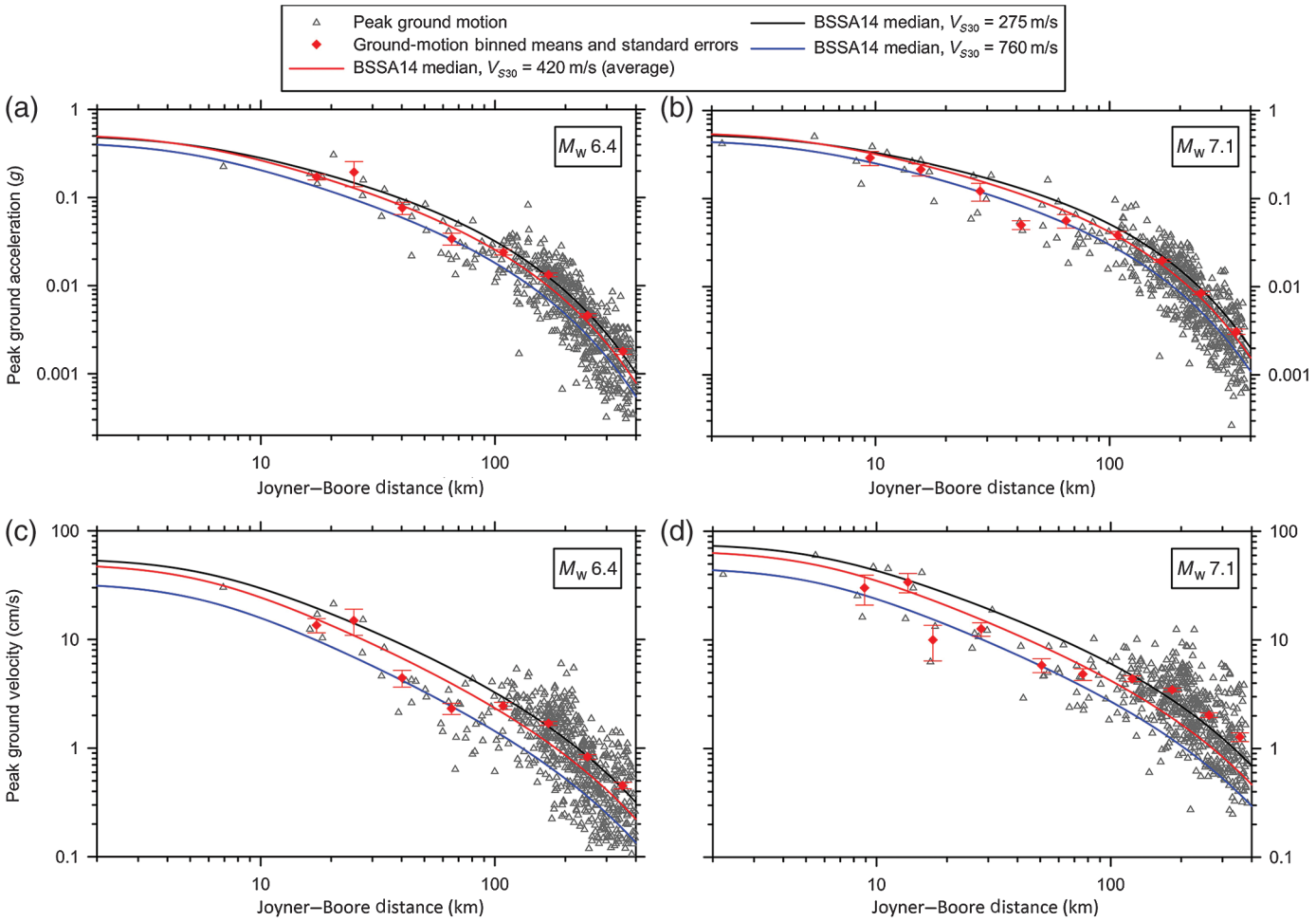

spectral ratios (HVSRs). Single-station HVSRs (sometimes referred to as HVEQ, to distinguish between HV analysis of earthquake [EQ] recordings and HV analysis of ambient noise) have been shown to yield estimates of site response that are generally consistent with estimates from comparison of sediment and reference sites (Field and Jacob, 1995). The approach may not yield a reliable indication of the site transfer function but does generally provide a good indication of resonance peaks. For the Ridgecrest earthquakes, a single-station approach is needed because there is no closely spaced pair of sediment and rock stations that can be used to estimate site response using a reference station. At longer periods, these ratios will be controlled by a combination of source effects and long-period site effects, for example, directivity and basin effects, respectively. At high frequencies, they are expected to reflect primarily local site effects due to impedance contrasts and nonlinear behavior in the near-surface soil column, because horizontal ground motions are typically amplified more than vertical ground motions (see Field and Jacob, 1995).

We focus on seven near-field stations (Fig. 2a and Table 1). Of these, CLC and LRL are hard-rock sites (Fig. 2a), and CCC is a soft-rock site. Three stations, NP5419, Q0072, and SRT, are on deep alluvial sediments in the Indian Wells Valley

Figure 3. PGA for (a) M_W 6.4 foreshock and (b) M_W 7.1 mainshock, and peak ground velocity (PGV) for (c) M_W 6.4 foreshock and (d) M_W 7.1 mainshock. All values plotted against Joyner–Boore distance, with BSSA14 predictions shown for soft rock (blue), V_{S30} 420 m/s sediments (red), and V_{S30} 275 m/s sediments (black).

(Monastero *et al.*, 2002). Depth to basement is ~1.6 km near Ridgecrest, constrained by boreholes drilled to basement (A. Katzenstein, oral comm., 1996; see Hough, 1997). Station TOW2 is a thin alluvium site near the northern edge of the Indian Wells Valley. To compute Fourier acceleration spectra, for both the foreshock and the mainshock, at each station we use a 40 s whole-record window, apply a 5% Hanning taper, calculate a Fourier transform, and apply median-point smoothing over a half-width of 20 points (0.49 Hz). We calculate HVSRs for both horizontal components and average them to obtain an average HV ratio at each station. For the mainshock and aftershock, the signal is at least two orders of magnitude higher than the pre-event noise level over the frequency range 0.1–10 Hz. HVSR at each station is found to be consistent in shape and amplitude for the three deep alluvium and the three rock stations (Fig. 4a,b); ratios from both sets of three stations are further averaged within 0.3–25 Hz to obtain

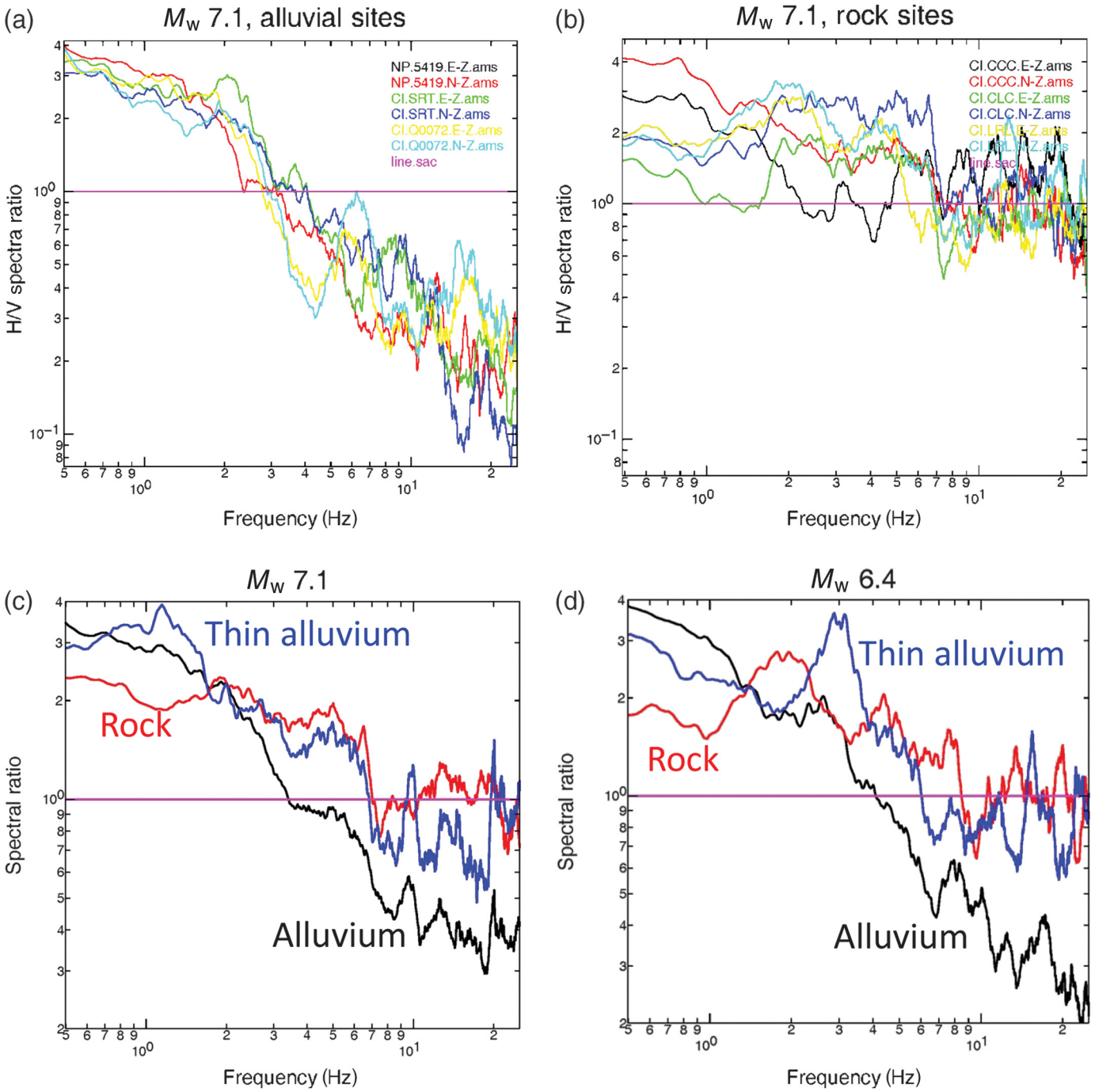

an average HVSR for near-field alluvial and hard-rock sites (Fig. 4c,d).

The average HVSR for the foreshock and mainshock are consistent in shape and amplitude (Fig. 4). The average HVSR at rock sites is close to two between 0.3, and ~6 Hz, and close to one between 6 and 25 Hz. (HVSRs at station CCC are higher than other rock sites between 0.5 and 1.0 Hz, which could reflect directivity.) The average HVSR at alluvial sites is higher (closer to a factor of 3) at frequencies below ~2 Hz but decreases sharply above 2 Hz, falling below 1 for frequencies above 3 Hz. Figure 4c,d suggests that, at deep and thin alluvial

Figure 4. (a) Average horizontal-to-vertical spectral ratio (HVSR) for the M_w 7.1 mainshock, calculated for each station as an average of the ratios using the individual horizontal components, for three alluvial sites (CI0072, NP5419, and SRT). Pink line indicates unity and (b) three rock sites (LRL, CLC, and CCC). (c) Average mainshock HVSR for all deep alluvium sites (black line), all rock sites (red line), and one thin alluvium site (blue line). Pink line indicates a value of 1. (d) Same results as shown in (c), for M_w 6.4 foreshock.

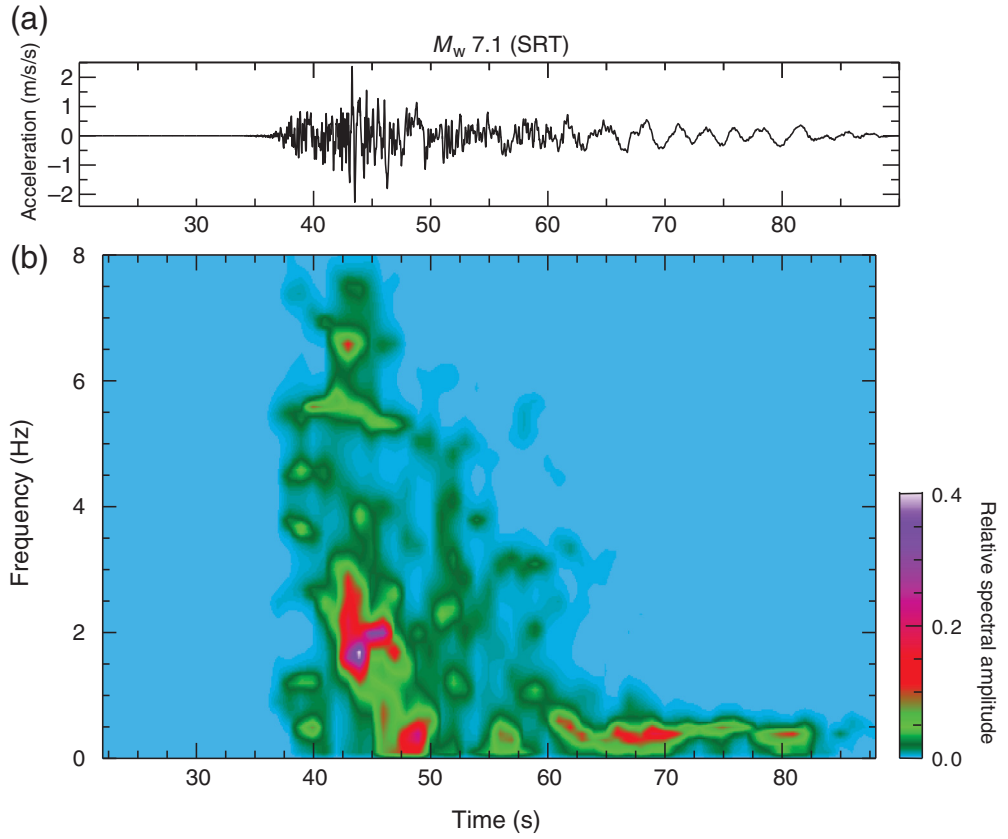

Figure 5. (a) Mainshock acceleration in meters per square second recorded on the north–south component at station SRT in Ridgecrest. (b) Relative frequency content (*Y* axis) as a function of time.

sites, energy at low frequencies, between ~0.5 and 2 Hz, is amplified, whereas energy above ~3 Hz is deamplified. This deamplification of ground motions coincides with the frequency band that generally controls macroseismic intensities (Sokolov and Cherov, 1998).

One can also consider the evolution of the frequency content of shaking throughout the strong-motion recordings of the mainshock, which can also provide evidence of nonlinearity (e.g., Dixit *et al.*, 2015). We calculate spectra within 4 s windows, calculated at time steps of 1 s; the resulting spectrogram for station SRT, on deep alluvium in Ridgecrest (Fig. 5) shows that energy above 2 Hz was recorded during the first 5–10 s of the *S*-wave group but not during the continuing strong motion (i.e., after ~47 s on the record in Fig. 5). It is possible that later arriving energy was more attenuated, and likely that anelastic attenuation did play some role in controlling high-frequency shaking. The diminution of high-frequency energy by attenuation would be gradual, however, whereas the observed drop is notably abrupt.

Although full analysis of recorded moderate aftershocks is beyond the scope of this initial report, we repeat the HVSR analysis of recordings of two smaller aftershocks, M_w 4.5 aftershock that occurred at 19:21:32 on 4 July, approximately two hours after the M_w 6.4 (Fig. 6a), an M_w 4.2 event at 20:09:51 on 10 July (Fig. 6b), and the immediate M_w 4.0 foreshock to the M_w 6.4 event on 4 July (Fig. 6c). All of these events were well recorded at six stations, with signal-to-noise ratios exceeding 10 between at least 0.5 and 25 Hz. The average HVSR at two sediment sites, SRT and Q0072, dips below 1 at high frequencies, but all HVSR are higher at frequencies between 3–4 and 10 Hz for the smaller events than the average HVSR at sediment sites for the two large events (Fig. 6d). We note that 3–10 Hz is the key frequency range of engineering concern for small structures.

Finally, we analyze four M_w 3.8–4.9 aftershocks from the 1995 Ridgecrest earthquake sequence (Table 3; Hough, 1997) recorded by a portable digital instrument installed at station RC1, shown on Figure 2a. These data were described and analyzed by Hough (1997), who developed a single-station multiple-empirical Greens' function (mEGF) method to estimate source, path, and site effects. Because the mEGF method involves fewer assumptions than the HVSR method, it is illustrative to consider how HVSR analysis of the 1995 events compares with the mEGF results. Repeating the HVSR analysis used to analyze events in this study, the average HVSR differs from the HVSR at sediment sites estimated in this study, for all four events analyzed. Clear resonance peaks around 2–3, 5–6, and ~9 Hz are evident in the HVSR for the 1995 events (Fig. 7), consistent with site response estimated by Hough (1997) using the mEGF method. This consistency provides a measure of validation for the HVSR method used in this study. Although peaks are suggested at similar frequencies in the HVSR of 2019 events analyzed for this study, they are subdued. Also, we note that the HVSRs for earlier events are consistently above 1.0 at frequencies up to 10 Hz.

Given a depth to basement H of ~1.6 km, the fundamental 1D resonance mode, $T = 4H/V_S$, is predicted to be around 2–3 s. This resonance is visually apparent in strong-motion recordings of both the foreshock and mainshock from stations in and around Ridgecrest (Fig. 5) and is generally consistent with observed low-frequency amplification at the sediment

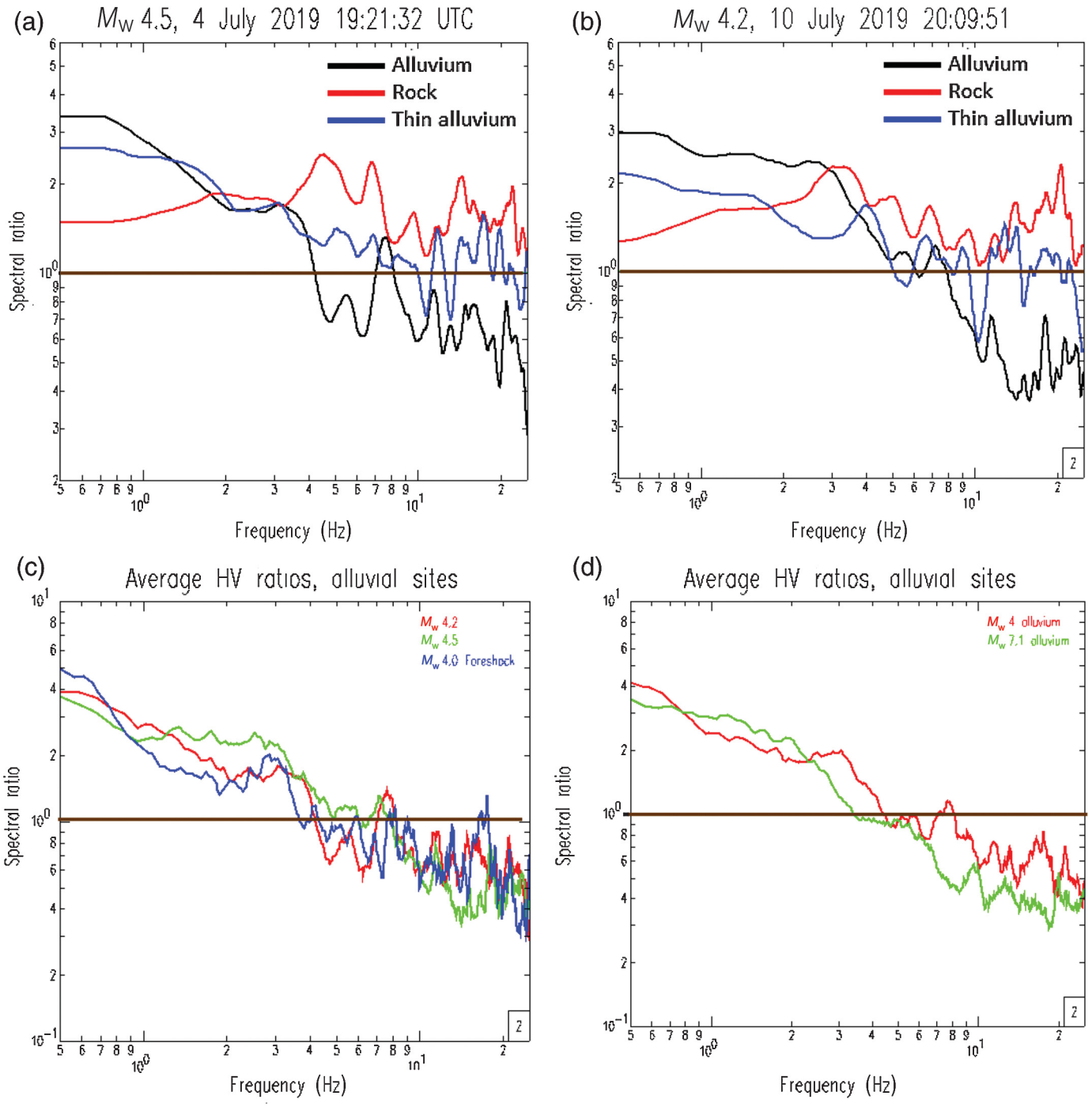

Figure 6. (a) Average HVSR for three rock sites (red line), two deep alluvial sites (black line), and one thin alluvium site (blue line) from recordings of an M_w 4.5 aftershock on 4 July; (b) similar plot from recordings of an M_w 4.2 aftershock on 10 July; (c) comparison of average HVSR for alluvial sites for M_w 4.2 aftershock (red), M_w 4.5 aftershock (green), and M_w 4.0 foreshock (blue); and (d) average of HVSRs calculated for three small events recorded at alluvial sites (Fig. 5c) (red) and HVSR for M_w 7.1 mainshock recorded at alluvial sites (green). Brown line in all panels indicates unity.

sites considered in this study (Figs. 5 and 6). The higher apparent resonance modes evident in Figure 6 suggest response of a shallower low-V_{S30} layer, as discussed by Hough (1997). These peaks are subdued or absent in HVSRs calculated for 2019 events analyzed in this study. We discuss this discrepancy in a later section.

Displaced Rocks

Finally, we consider observed environmental effects that can provide a quantitative estimate of PGA. Some environmental effects, including rock falls and liquefaction, are recognized to

TABLE 3
Moderate 1995 Aftershocks Analyzed in This Study

Julian Day	Hours	Minute	Latitude (°N)	Longitude (°W)	M_w
242	15	54	35.7957	117.6400	4.0
264	23	48	35.7613	117.6425	4.0
268	04	47	35.8087	117.6162	4.9
275	00	10	35.8095	117.6455	3.8

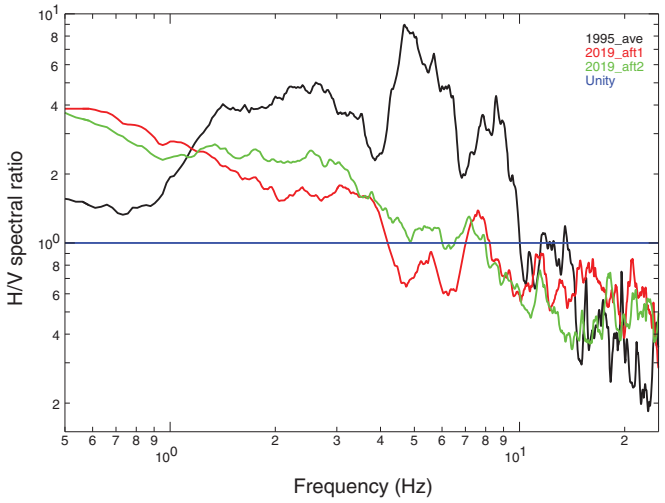

Figure 7. HVSRs for M_w 4.5 and 4.2 aftershocks analyzed in this study (both horizontals from all alluvial stations averaged; red and green lines), and average HVSR for four M_w 3.8–4.9 aftershocks of the 1995 Ridgecrest earthquake recorded at an alluvial site (black line). Blue line indicates value of unity.

be generally unreliable indicators of shaking severity (e.g., Ambraseys, 1971; Ambraseys, 1983); we do not attempt to consider such observations here. Observations of displaced rigid objects, either natural or man-made can, however, provide a quantitative estimate of PGA (e.g., Clark, 1972; Bolt and Hansen, 1977; Michael *et al.*, 2002; Hough *et al.*, 2012). Interpretation of such observations is more straightforward when objects are displaced on level ground (Michael *et al.*, 2002).

Following the M_w 7.1 mainshock, displaced rocks were observed during geological field surveys in three locations (Fig. 2a). Near the northwestern terminus of the rupture (FR1), in which a number of cross faults were observed, a site with a number of displaced rocks was observed near a right-stepover along one of the cross faults. Some rocks were apparently toppled from pedestals, and some were found displaced from their original position with no evidence that they slid or rolled on the ground (Fig. 8a).

A second concentration of displaced rocks, including some that were apparently flung (Figs. 2a and 8b), was found near a restraining stepover toward the southern end of the mainshock rupture (FR2). At this site, a small number of flung rocks were observed over an area approximately 1 × 1 km. Because both of these flung-rock locations are in proximity to the M_w 7.1 mainshock, we assume they were displaced by this earthquake, not the foreshock. At a third location, FR3, along the mainshock rupture in proximity to the edge of the up-thrown side of the fault, plates of the dry lakebed surface were clearly flung into the air and flipped over, landing as much as 2 m from their original location (Haddon *et al.*, 2019; Fig. 8d).

Flung, or flying, rocks or other objects nominally imply PGA values above 1*g*, or MMI ≥ 10. The relatively low number of flung rocks at FR2 suggests that PGA in this location was not consistently above 1*g* over the broad area, but rather that high-frequency accelerations reached 1*g* in some much localized areas. The first-order implications of the observations are also not unambiguous. It has been shown, for example, that the response of elastic systems can conspire to cause objects to be thrown into the air at PGA values below 1*g* (Bolt and Hansen, 1977). Although it is not clear to what extent the physical model considered by Bolt and Hansen (1977) applies to rocks sitting on the desert floor, more detailed analysis may be useful to better constrain PGA estimates at the three locations where rocks were apparently flung. For the purposes of this study, we do not attempt to estimate a precise estimate of PGA, but rather to use the observations to estimate MMI. To help constrain the intensity values at FR1 and FR2, we visited station CCC, which recorded the largest instrumental PGA value from the mainshock, 0.57*g*. This station is located several kilometers south-southeast of the southern terminus of the mainshock rupture. In the vicinity of this station, there was evidence for local rock falls from an east–west-trending ridge to the immediate north of the station but no evidence for displaced rocks either on the flatter ground immediately north of the ridge or along other ridges within a few 100 m of the station. As at FR2, there are many small rocks in this location that are not cemented to the desert floor (Fig. 8c). We, therefore, conclude that PGA near FR2 was higher than 0.57*g*, but not pervasively over 1*g*. Using the Worden *et al.* (2012) acceleration–intensity IPE, PGA values between 0.6 and 1*g* correspond to intensities of 8.65–9.47. We, therefore, assign intensity 9 ± 0.5 at this location. At FR1, where there was more pervasive disturbance of rocks and plates, we conclude that PGA was higher than at FR2 and assign intensity 10 ± 0.5. We also assign intensity 10 ± 0.5 at FR3, where there is compelling evidence that slabs of desert pavement were flung in the air. We note, however, that PGA values greater than 1*g* are inferred only in immediate proximity (i.e., a few meters to tens of meters) to the up-thrown fault block; the recorded PGA values at station CLC, a hard-rock site approximately 2 km from FR3, were 3.53–4.74 m/s^2 (36%–48%*g*).

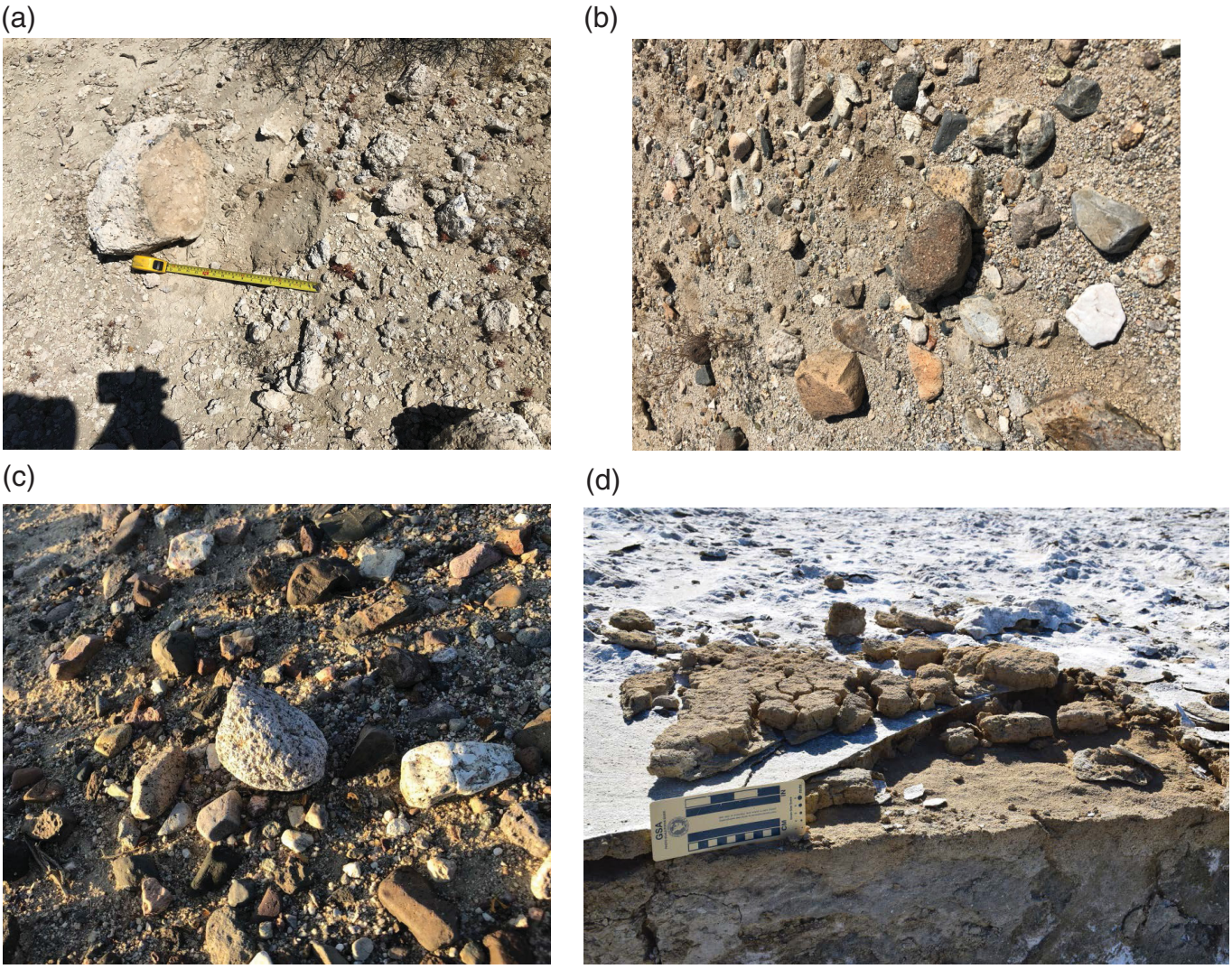

Figure 8. (a). Rock near the northern mainshock terminus apparently flung and turned over by the M_w 7.1 mainshock, (b) rock near the southern mainshock terminus apparently flung laterally by the M_w 7.1 mainshock, (c) rocks on the desert floor within 100 m of station CCC, which showed no indications of displacement, and (d) along mainshock rupture (FR3), slabs of rock flung into the air and flipped over.

Discussion and Conclusions

Although near-field observations remain sparse due to the relatively remote location of the M_w 7.1 Ridgecrest mainshock, a combination of noninstrumental and instrumental data provides the most robust characterization of near-field ground motions. Using all available data, we conclude that even in proximity to the mainshock rupture, near-fault ground motions were generally below 1*g*, equivalent to at most MMI 9. Near-field shaking appears to have neared and perhaps even exceeded 1*g* in three locations in proximity to the mapped mainshock surface rupture. Two of these locations coincide with zones of complexity in the mapped surface trace (e.g., Brandenberg *et al.*, 2019); we speculate that rupture complexity in these areas might have generated locally large high-frequency radiation.

In Ridgecrest, the closest large population center to the earthquakes, intensities during the M_w 7.1 mainshock were generally higher than from the M_w 6.4 foreshock, but the difference is lower than predicted by the IPE determined by Atkinson and Wald (2007). Source-controlled directivity and nearest-fault distance may account for some of this difference; the M_w 6.4 primarily involved rupture on a southwest–northeast-trending cross fault, with rupture toward the southern edge of Ridgecrest.

Consideration of single-station HVSRs for the mainshock and aftershock reveal, however, a depletion of horizontal high-frequency energy at alluvial sites during the mainshock. The depletion at frequencies higher than ~3 Hz is strongest at deep alluvium sites and not observed at soft- and hard-rock sites in proximity to the mainshock rupture. The correspondence with site geology, and the consistency of results for both the mainshock and foreshock, suggests that ground motions at

frequencies above ~3 Hz were deamplified by a pervasive nonlinear response of alluvial Indian Wells Valley sediments. Nonlinear sediment response, or the increase in soil damping with increasing excitation strength, has been observed in many large earthquakes. For example, a similar deamplification was observed in the Kathmandu Valley during the 2015 M_w 7.8 Gorkha, Nepal, earthquake (Dixit *et al.*, 2015; Rajaure *et al.*, 2017), where damage to small vernacular structures was also lower than expected given the magnitude of the earthquake and the distance from Kathmandu to the fault rupture. Evidence of pervasive nonlinear response has been presented by other studies of large earthquakes (Chin and Aki, 1991; Field *et al.*, 1997; Rubinstein and Beroza, 2004). Looking back at damage observations from the 1993 Long Beach, California, earthquake, Trifunac (2003) concluded that pervasive nonlinear response at soft-sediment sites near Long Beach deamplified shaking at frequencies that would have been damaging to small, unreinforced masonry structures in proximity to the rupture.

Modern empirical ground-motion models for V_{S30}-based site response typically model some nonlinearity when the ground motion is larger than a certain value. The site response model of Seyhan and Stewart (2014), adopted as the site term in the BSSA14 GMPE, was developed using a combination of 1D equivalent-linear ground response simulations and the NGA-West2 database of recorded ground motions from shallow earthquakes inactive tectonic regions, and thus should be applicable to the Ridgecrest region. At frequencies greater than 3.3 Hz, ground motions at soft soil sites ($V_{S30} < 500$ m/s) are modeled with nonlinear terms that deamplify the ground motion when the rock PGA is larger than 10%g. This model feature is shown by the BSSA14 predictions in Figure 3; at longer periods (e.g., PGV, Fig. 3c,d) and distances where ground motions are lower (~100 km), the model predictions continue to scale linearly with V_{S30} decreasing beyond 500 m/s. Comparatively, for short periods (e.g., PGA, Fig. 3a,b) and close distances with larger ground motions (~10–40 km), the model predictions do not increase, or increase marginally, with decreasing V_{S30}. These BSSA14 model predictions indicate that given the strength of shaking, some nonlinearity was expected for the short-period ground motions at near-source, slow V_{S30} sites during both the M_w 6.4 and 7.1 events. Although in-depth investigations of near-surface velocity structure have not yet been carried out for the stations considered, several of the alluvium and thin alluvium sites we analyze appear to meet the criteria of soft site conditions and large rock ground motions, and qualitatively the model agrees with the nonlinearity we observe at these locations. Further in-depth investigation will be needed to make quantitative comparisons between the observations and published models and to better constrain near-surface velocity structure.

The different character of the HVSR estimated for moderate aftershocks of the 1995 Ridgecrest earthquake is intriguing. It is possible that site response is different at station RC1 than at the alluvial sites where the 2019 events were recorded, although the consistency of HVSR at all deep-alluvial sites (e.g., Fig. 4a) argues against this interpretation. It is also possible that sediment response at deep alluvial sites in the Indian Wells Valley has remained nonlinear during the days following the initial large events (Sawazaki *et al.*, 2006). The consistency of the HVSR results for the M_w 4.0 foreshock argues against this interpretation, but there is a suggestion that this event had somewhat more distinct high-frequency resonance peaks than did the M_w 7.1 mainshock or M_w 6.4 foreshock (Fig. 6c). We note that prolonged diminution of sediment-controlled resonance peaks, such as that suggested by Figure 6, could help explain the observation that aftershock ground motions are generally lower than mainshock ground motions (e.g., Abrahamson and Silva, 2008). In any case, the consistent HVSR results for the 1995 events with the results of Hough (1997) provides a measure of validation for the HVSR method. In-depth analysis of a larger set of small-to-moderate events from the 2019 sequence will be needed to further explore these issues, including the possibility that site response evolved over time following the initial large earthquakes.

Further study will also be needed to consider the role of other factors that might have controlled near-field ground motions, including nonlinear rupture processes (e.g., Gabriel *et al.*, 2013), directivity, and stress drop (e.g., Hanks and Johnston, 1992; Hough, 2014). In addition, observations from other surface-rupturing crustal earthquakes show systematically weaker high-frequency ground-motion levels compared with ruptures that do not break the ground surface (Kagawa *et al.*, 2004; Shearer *et al.*, 2006; Pitarka *et al.*, 2009). Similar differences in shallow and deep rupture characteristics have also been documented for large subduction zone events (e.g., Wei *et al.*, 2012; Frankel, 2017). This behavior can be explained by velocity strengthening friction during fault rupture at shallow depths (e.g., Marone and Scholz, 1988; Dalguer *et al.*, 2008), which can be modeled kinematically as a reduction in rupture speed and lengthening of the slip rise time in the near surface portion of the rupture (e.g., Graves and Pitarka, 2016).

The similarity of HVSRs for the M_w 6.4 foreshock and M_w 7.1 mainshock argues against significant influence by directivity. The modest macroseismic effects observed near the southwest terminus of the M_w 6.4 foreshock, at BLM facilities surveyed for this study, do suggest, however, that, at least in some locations along the rupture, shallow high-frequency radiation may have been muted by source effects in addition to site response. In any case, the depletion of energy at frequencies above 3 Hz explains the relatively limited damage in Ridgecrest, including the lack of damage to chimneys and roof-top evaporative coolers. All of the structures in this and neighboring smaller towns are 1–2 stories tall and would have been affected by shaking in the 3–10 Hz range. Shaking at frequencies lower than ~3 Hz was amplified by sediments in

the Indian Wells Valley and would have been potentially damaging to structures taller than three stories, but no such structures existed. The results from Ridgecrest, like those from the 2015 Gorkha earthquake, suggest that small structures on alluvial sites will generally undergo less severe shaking than predicted from linear extrapolation of results from weak ground motion, which is qualitatively captured in nonlinear site response functions. The results do, however, underscore the concern for larger structures, the fundamental periods of which are closer to lower frequency amplification effects. During the Ridgecrest sequence, long-period amplification may have contributed to damage to some local buildings with large spatial footprints, including the local theater and Dollar Store.

Data and Resources

Ground-motion recordings of the foreshock and mainshock, peak acceleration values for both events, and site characterization information for the stations listed in Table 1 can be downloaded from https://strongmotioncenter.org (last accessed July 2019). "Did You Feel It?" (DYFI) intensity data can be downloaded from https://earthquake.usgs.gov/earthquakes/eventpage/ci38443183/dyfi/intensity and https://earthquake.usgs.gov/earthquakes/eventpage/ci38457511/dyfi/intensity (both last accessed July 2019) for the foreshock and mainshock, respectively. News reports about damage on the China Lake Naval Air Weapons Station were downloaded from https://www.navytimes.com/news/your-navy/2019/08/12/china-lake-repair-costs-might-top-2-billion/ (last accessed September 2019). Evaluating damage at China Lake base school is available at https://www.bakersfield.com/multimedia/photo-galleries/photo-gallery-evaluating-damage-at-china-lake-base-school/collection_91115390-a2a5-11e9-944f-977e60c2b209.html (last accessed September 2019). The information about the Navy facing a billion dollar tab is available at https://news.usni.org/2019/08/21/navy-facing-billion-dollar-tab-years-to-get-china-lake-fully-operational-after-quake (last accessed September 2019).

Acknowledgments

The authors thank Paul Friberg for supplying an ah2sac code to help us resuscitate data from the 1995 Ridgecrest sequence, and the many residents of Ridgecrest who provided information about earthquake effects. Assistance from Ken Sanger and Skip Graff, and the staffs of the Maturango Museum, Ridgecrest Animal Shelter, and Ridgecrest Independent are acknowledged with appreciation. The general cooperation of the Naval Air Weapons stations is acknowledged with appreciation. The authors thank Nicholas van der Elst, Brad Aagaard, Shane Detweiller, and two anonymous reviewers for their constructive reviews of this article, and Alison Bent for her stewardship of the journal.

References

Abrahamson, N., and W. Silva (2008). Summary of the Abrahamson & Silva NGA ground-motion relations, *Earthq. Spectra* **24,** no. 1, 67–97.

Ambraseys, N. (1983). Notes on historical seismicity, *Bull. Seismol. Soc. Am.* **73,** no. 6A, 1917–1920.

Ambraseys, N. N. (1971). Value of historical records of earthquakes, *Nature* **232,** no. 5310, 375–379.

Atkinson, G. M., and D. J. Wald (2007). "Did You Feel It?" intensity data: A surprisingly good measure of earthquake ground motion, *Seismol. Res. Lett.* **78,** 362–368.

Boatwright, J., and E. Phillips (2017). Exploiting the demographics of "Did You Feel It?" responses to estimate the felt area of moderate earthquakes in California, *Seismol. Res. Lett.* **88,** no. 2A, 335–341.

Bolt, B. A., and R. A. Hansen (1977). The upthrow of objects in earthquakes, *Bull. Seismol. Soc. Am.* **67,** no. 5, 1415–1427.

Boore, D. M., J. P. Stewart, E. Seyhan, and G. M. Atkinson (2014). NGA-West2 equations for predicting PGA, PGV, and 5% damped PSA for shallow crustal earthquakes, *Earthq. Spectra* **30,** no. 3, 1057–1085.

Brandenberg, S. J., P. Wang, C. C. Nweke, K. Hudson, S. Mazzoni, Y. Bozorgnia, K. W. Hudnut, C. A. Davis, S. K. Ahdi, F. Zareian, *et al.* (2019). Preliminary report on engineering and geological effects of the July 2019 Ridgecrest earthquake sequence, *U.S. Geol. Surv.* doi: 10.18118/G6H66K.

Brazlee, R. J. (1979). Evaluation of modified Mercalli intensity scale for earthquakes using distance as a determinant, *Bull. Seismol. Soc. Am.* **69,** no. 3, 911–924.

Chin, B. H., and K. Aki (1991). Simultaneous study of the source, path, and site effects on strong ground motion during the 1989 Loma Prieta earthquake: A preliminary result on pervasive nonlinear site effects, *Bull. Seismol. Soc. Am.* **81,** no. 5, 1859–1884.

Clark, M. (1972). Surface rupture along the Coyote Creek fault, in *The Borrego Mountain Earthquake of April 9, 1968: U.S. Geol. Surv. Profess. Pap. 787*, 55–86.

Dalguer, L. A., H. Miyake, S. M. Day, and K. Irikura (2008). Surface rupturing and buried dynamic rupture models calibrated with statistical observations of past earthquakes, *Bull. Seismol. Soc. Am.* **98,** 1147–1161.

Dengler, L. A., and J. W. Dewey (1998). An intensity survey of households affected by the Northridge, California, earthquake of 17 January, 1994, *Bull. Seismol. Soc. Am.* **88,** 441–462.

Dixit, A. M., A. Ringler, D. Sumy, E. Cochran, S. E. Hough, S. S. Martin, S. Gibbons, J. Luetgert, J. Galetzka, S. N. Shrestha, *et al.* (2015). Strong-motion observations of the M 7.8 Gorkha, Nepal, earthquake sequence and development of the N-shake strong-motion network, *Seismol. Res. Lett.* **86,** no. 6, 1533–1539, doi: 10.1785/0220150146.

Field, E. H., and K. H. Jacob (1995). A comparison and test of various site-response estimation techniques, including three that are not reference-site dependent, *Bull. Seismol. Soc. Am.* **85,** no. 4, 1127–1143.

Field, E. H., P. A. Johnson, I. A. Beresnev, and Y. Zeng (1997). Nonlinear ground-motion amplification by sediments during the 1994 Northridge earthquake, *Nature* **390,** no. 6660, 599.

Frankel, A. (2017). Modeling strong-motion recordings of the 2010 Mw 8.8 Maule, Chile, earthquake with high stress-drop subevents and background slip, *Bull. Seismol. Soc. Am.* **107,** no. 1, 372–386, doi: 10.1785/0120160127.

Gabriel, A. A., J. P. Ampuero, L. A. Dalguer, and P. M. Mai (2013). Source properties of dynamic rupture pulses with off-fault plasticity, *J. Geophys. Res.* **118,** no. 8, 4117–4126.

Graves, R. W., and A. Pitarka (2016). Kinematic ground motion simulations on rough faults including effects of 3D stochastic velocity

perturbations, *Bull. Seismol. Soc. Am.* **106,** no. 5, doi: 10.1785/0120160088.

Gregor, N., N. A. Abrahamson, G. M. Atkinson, D. M. Boore, Y. Bozorgnia, K. W. Campbell, and B. S.-J. Chiou (2014). Comparison of NGA-West2 GMPEs, *Earthq. Spectra* **30,** no. 3, 1179–1197.

Grünthal, G. (Editor) (1998). *The European Macroseismic Scale EMS-98*, Vol. 15, Conseil de l'Europe, Cahiers du Centre Europeén de Geodynamique et de Seismoligie, Luxembourg.

Haddon, E. K., S. E. Bennett, J. R. Patton, K. K. Kendrick, D. D. Oglesby, B. Olsen, C. B. DuRoss, and A. Pickering (2019). Coseismic variations in slip orientation from curved striations and projectile play soils during the 2019 M7.1 Ridgecrest earthquake (abstract), *Southern California Earthquake Center Annual Meeting*, Palm Springs, California, 8–11 September 2019.

Hanks, T. C., and A. C. Johnston (1992). Common features of the excitation and propagation of strong ground motion for North American earthquakes, *Bull. Seismol. Soc. Am.* **82,** no. 1, 1–23.

Hauksson, E., K. Felzer, D. Given, M. Giveon, S. E. Hough, K. Hutton, H. Kanamori, V. Sevilgen, S. Wei, and A. Yong (2008). Preliminary report on the 29 July 2008 Mw 5.4 Chino Hills, eastern Los Angeles basin, California, earthquake sequence, *Seismol. Res. Lett.* **79,** no. 6, 855–866.

Hough, S. E. (1997). Empirical Green's function analysis: Taking the next step, *J. Geophys. Res.* **102,** no. B3, 5369–5384.

Hough, S. E. (2000). On the scientific value of unscientific data, *Seismol. Res. Lett.* **71,** 483–485.

Hough, S. E. (2014). Shaking from injection-induced earthquakes in the central and eastern United States, *Bull. Seismol. Soc. Am.* **104,** 2619–2626, doi: 10.1785/0120140099.

Hough, S. E., and M. Page (2011). Towards a consistent model for strain accrual and release for the New Madrid Seismic Zone, central United States, *J. Geophys. Res.* **116,** no. B3, doi: 10.1029/2010JB007783.

Hough, S. E., T. Taniguchi, and J.-R. Altidor (2012). Estimation of peak ground acceleration from horizontal rigid body displacement: A case study in Port-au-Prince, *Bull. Seismol. Soc. Am.* **102,** no. 6, 2704–2713.

Joyner, W. B., and D. M. Boore (1981). Peak horizontal acceleration and velocity from strong-motion records including records from the 1979 Imperial Valley, California, earthquake, *Bull. Seismol. Soc. Am.* **71,** no. 6, 2011–2038.

Kagawa, T., K. Irikura, and P. Somerville (2004). Differences in ground motion and fault rupture process between surface and buried rupture earthquakes, *Earth Planets Space* **56,** no. 1, 3–14.

Lin, R. (2019). Ridgecrest earthquake mystery: Why so little destruction from huge temblors?, *Los Angeles Times*, 10 July.

Marone, C., and C. H. Scholz (1988). The depth of seismic faulting and the upper transition from stable to unstable slip regimes, *Geophys. Res. Lett.* **15,** no. 6, 621–624.

Michael, A. J., S. L. Ross, and H. D. Stenner (2002). Displaced rocks, strong motion, and the mechanics of shallow faulting associated with the 1999 Hector Mine, California, earthquake, *Bull. Seismol. Soc. Am.* **92,** no. 4, 1561–1569.

Monastero, F. C., J. D. Walker, A. M. Katzenstein, A. E. Sabin, A. F. Glazner, and J. M. Bartley (2002). Neogene evolution of the Indian Wells Valley, east-central California, in *Geologic Evolution of the Mojave Desert and Southwestern Basin and Range*, A. F. Glazner, J. D. Walker, and J. M. Bartley (Editors), Geol. Soc. Am. Memoir, Vol. 195, 199–228.

Musson, R. M., G. Grünthal, and M. Stucchi (2010). The comparison of macroseismic intensity scales, *J. Seismol.* **14,** no. 2, 413–428.

Pitarka, A., L. A. Dalguer, S. M. Day, P. G. Somerville, and K. Dan (2009). Numerical study of ground-motion differences between buried rupturing and surface-rupturing earthquakes, *Bull. Seismol. Soc. Am.* **99,** no. 3, 1521–1537.

Rajaure, S., D. Asimaki, E. Thompson, S. E. Hough, P. Ampuero, S. S. Martin, A. Inbal, and M. Dhital (2017). Characterizing the Kathmandu Valley sediment response through strong motion recordings of the 2015 Gorkha earthquake sequence, *Tectonophysics* **714/715,** doi: 10.1016/j.tecto.2016.09.030.

Ross, Z. E., B. Idini, Z. Jia, O. L. Stephenson, M. Zhong, X. Wang, Z. Zhan, M. Simons, E. J. Fielding, S. H. Yun, and E. Hauksson (2019). Hierarchical interlocked orthogonal faulting in the 2019 Ridgecrest earthquake sequence, *Science* **366,** no. 6463, 346–351.

Rubinstein, J. L., and G. C. Beroza (2004). Evidence for widespread nonlinear strong ground motion in the Mw6.9 Loma Prieta earthquake, *Bull. Seismol. Soc. Am.* **94,** no. 5, 1595–1608.

Sawazaki, K., H. Sato, H. Nakahara, and T. Nishimura (2006). Temporal change in site response caused by earthquake strong motion as revealed from coda spectral ratio measurement, *Geophys. Res. Lett.* **33,** no. 21, doi: 10.1029/2006GL027938.

Seyhan, E., and J. P. Stewart (2014). Semi-empirical nonlinear site amplification from NGA-West2 data and simulations, *Earthq. Spectra* **30,** no. 3, 1241–1256, doi: 10.1193/063013EQS181M.

Shearer, P. M., G. A. Prieto, and E. Hauksson (2006). Comprehensive analysis of earthquake source spectra in southern California, *J. Geophys. Res.* **111,** no. B06303, doi: 10.1029/2005JB003979.

Sokolov, V. Y., and Y. K. Cherov (1998). On the correlation of seismic intensity with Fourier amplitude spectra, *Earthq. Spectra* **14,** 679–694, doi: 10.1193/1.1586022.

Trifunac, M. D. (2003). Nonlinear soil response as a natural passive isolation mechanism. The 1933 Long Beach, California, earthquake, *Soil Dynam. Earthq. Eng.* **23,** 549–562.

Wei, S., R. Graves, D. Helmberger, J.-P. Avouac, and J. Jiang (2012). Sources of shaking and flooding during the Tohoku-Oki earthquake: A mixture of rupture styles, *Earth Planet. Sci. Lett.* **333,** 91–100, doi: 10.1016/j.epsl.2012.04.006.

Wald, D. J., V. Quitoriano, L. Dengler, and J. W. Dewey (1999). Utilization of the internet for rapid community intensity maps, *Seismol. Res. Lett.* 70, no. 6, 680–697, doi: 10.1785/gssrl.70.6.680..

Worden, C., and D. Wald (2016). Shakemap manual online: Technical manual, user's guide, and software guide, available at http://usgs.github.io/shakemap (last accessed September 2019).

Worden, C. B., M. C. Gerstenberger, D. A. Rhoades, and D. J. Wald (2012). Probabilistic relationships between ground-motion parameters and modified Mercalli intensity in California, *Bull. Seismol. Soc. Am.* **102,** 204–221, doi: 10.1785/0120110156.

Manuscript received 27 September 2019
Published online 26 February 2020